Materials and Design 136 (2017) 127–136

Contents lists available at ScienceDirect

Materials and Design

journal homepage: www.elsevier.com/locate/matdes

Synthesis and characterization of nano magnesium oxide impregnated granular activated carbon composite for H_2S removal applications

Induni W. Siriwardane [a,b], Ranodhi Udangawa [a,b,1], Rohini M. de Silva [a], A.R. Kumarasinghe [b,c,d], Robert G. Acres [d,2], Ananda Hettiarachchi [b], Gehan A.J. Amaratunga [b,e], K.M. Nalin de Silva [a,b,*]

[a] Department of Chemistry, University of Colombo, Colombo 00300, Sri Lanka
[b] Sri Lanka Institute of Nanotechnology (SLINTEC), Nanotechnology and Science Park, Mahenwatte, Pitipana, Homagama, Sri Lanka
[c] Department of Physics, Faculty of Applied Sciences, University of Sri Jayawardenapura, Nugegoda, Sri Lanka
[d] Material Science Beamline, Elettra-Sincrotrone Trieste S.C.p.A di Interesse Nationale, Strada Statale, 14-km 163,5 in AREA Science Park, 34149 Basovizza, Trieste, Italy
[e] Department of Engineering, University of Cambridge, 9, J.J. Thomson Avenue, Cambridge CB3 0FA, UK

HIGHLIGHTS

- Composite of nano-MgO and granular activated carbon (GAC) was synthesised.
- Claims were supported by XRD, TGA, BET, UPS, NEXAFS, SEM, TEM and ICP-OES.
- The H_2S adsorption capacities were determined following the ASTM D6646 method.
- Composite showed more than five times higher H_2S adsorption capacity than virgin GAC.
- High capacity was attributed to both physical and chemical adsorption processes.

GRAPHICAL ABSTRACT

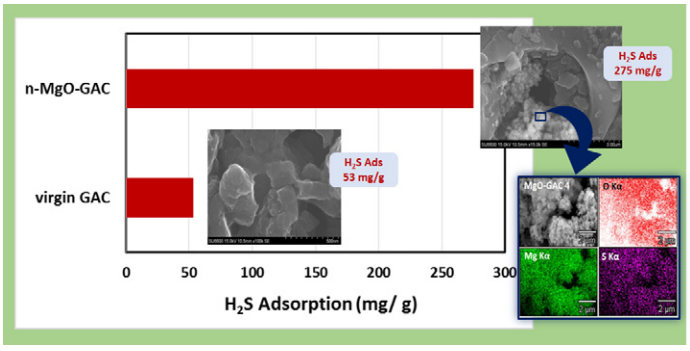

ARTICLE INFO

Article history:
Received 15 April 2017
Received in revised form 16 September 2017
Accepted 18 September 2017
Available online 21 September 2017

Keywords:
Nano MgO
Activated carbon
H_2S adsorption
NEXAFS

ABSTRACT

In this study, a composite of nano magnesium oxide (MgO) and granular activated carbon (GAC) was synthesized and analyzed for its H_2S adsorption capacity. The synthesis of composite involved a spray technique, which incorporates nano MgO even into micropores of GAC. The nanocomposite was characterized structurally and chemically, using scanning electron microscopy (SEM), X-ray diffraction (XRD), thermogravimetric analysis (TGA), N_2-BET adsorption studies, ultra-violet photoelectron spectroscopy (UPS) and near edge X-ray absorption fine structure spectroscopy (NEXAFS) and inductively coupled plasma optical emission spectroscopy (ICP-OES). The composite described herein showed more than five times higher H_2S adsorption capacity than the virgin GAC. The high adsorption capacity shown by the MgO-GAC composite could be attributed to the fact that the composite structure exploits both physical and chemical adsorption processes simultaneously. The physical adsorption was occured at the macro and mesoporous structure of GAC whereas as the chemical adsorption was at the nano-MgO site. The differential thermogravimetric (DTG) analysis evidenced that the main mode of chemical adsorption was the oxidation of H_2S, whereas a secondary metal supported addition mechanism was also shown to exist.

* Corresponding author at: Department of Chemistry, University of Colombo, Colombo 00300, Sri Lanka.
[1] Current address: Rensselaer Polytechnic Institute, New York, USA.
[2] Current address: Australian Synchrotron, Imaging and Medical Beamline, 800 Blackburn Road, Clayton, Victoria, 3168, Australia.

https://doi.org/10.1016/j.matdes.2017.09.034
0264-1275/

1. Introduction

Hydrogen sulfide (H_2S) is among the most widely discussed gaseous pollutants in the environment. The toxic effects of H_2S are observed on the nervous [1–3], respiratory [4,5], reproductive systems [6,7] and secondarily on eyes [3,8–10], skins [9], cardiovascular system [11,12], hepatic tissues [9], renal system [9], gastrointestinal system [9], immune system [5] and endocrine system [3]. The common rationale is that the toxicity of hydrogen sulfide is due to the inhibition of cytochrome oxidase [13]. However, the participation of reactive sulfur species in the mechanism of H_2S toxicity through depletion of glutathione and activation of oxygen to form reactive oxygen species have also been observed [13]. Hypoxia, respiratory insufficiencies, pulmonary edema and neurotoxic effects are some commonly reported impacts of exposure to acute levels of hydrogen sulfide gas [14,15]. As the toxic effects of hydrogen sulfide have become apparent, many mechanisms of removing hydrogen sulfide in gas streams have also been developed. Currently catalytic oxidation of H_2S using metal chelates is the widely commercialized method [16–18]. Zeolites [19,20], silica [21], titania [21] and specially developed resins [21] are some other materials used for large scale H_2S removal processes. Additionally, biofiltration is also being used for H_2S separation [22]. Further, the use of metals and their oxides for H_2S removal has been a widely explored area by many researchers [23–26].

Despite the methods mentioned above, activated carbon and their composites have also been among the effective options for H_2S removal for several decades. Among the wide variety of carbon based materials, activated carbon, activated carbon fibers [27] and activated carbon cloths [28] have been studied for the H_2S removal. The presence of a pore structure and high surface area, as well as functional groups such as COO^-, OH makes activated carbon, a suitable material for adsorption of foreign molecules [29,30]. Consequently, activated carbon is widely used in the removal of pollutants [31], and is one of the major components in water filters [32,33] and air filters [34–36]. It is used to filter a broad range of contaminants, such as volatile organic compounds [36,37], toxic gases such as SO_2 [38], H_2S [34,39–43] and certain heavy metal ions [31–33]. Further, its ability of desorbing the adsorbed gases at high temperatures has made it an attractive material to be used in gas filters.

The removal of H_2S by activated carbon can occur via several mechanisms [28,44]. The addition of sulfur on carbon sites or the substitution of oxygen atoms on carbon active sites by sulfur or adsorption of sulfur atoms by metals in a favorable addition reaction have been proposed. Therefore, incorporation of metals are favorable for H_2S adsorption and higher H_2S adsorption capacities have been observed with higher metal concentrations on the activated carbon species [44].

On the other hand, Yan et al. [45] explain a different facet for H_2S adsorption on activated carbons, suggesting three possible adsorption modes namely, physical adsorption, chemical adsorption and catalytic oxidation [45]. Many studies have explored the effects of dynamic conditions such as pH [46], humidity [47], adsorbent (activated carbon) properties [27,48] and adsorbate (H_2S) properties [44] in achieving the maximum H_2S adsorption using activated carbon based adsorbents.

Currently, chemical modifications on activated carbon are the major focus, in order to enhance its effectiveness in adsorption of H_2S. Most of these chemical modifications are based on proposed mechanisms of action. For example, treating carbon with alkaline material is shown to increase H_2S adsorption via an oxygen substitution mechanism are summarized [45,46,49]. Potassium iodide (KI) is another agent used to modify activated carbon in order to achieve selective adsorption of H_2S on to surface functional groups of carbon [49]. The introduction of nitrogen atoms by ammonia is also reported to increase H_2S adsorption capacity, not only by increasing the surface nitrogen groups but also by changing the distribution of oxygen groups and by changing the microporosity [50]. Further, the introduction of nitrogen functionality on carbon matrix via urea [51] and silica-polyamine [52] have also been reported. Moreover, the use of copper impregnated activated carbon for H_2S removal has also been reported [47]. However the exploitation of the metal group functionalities to enhance the synergistic adsorption effects is an area yet to be further explored. In this work a composite of nano MgO and GAC is fabricated to achieve improved adsorption properties. The ability of catalyze H_2S removal by magnesium hydroxide ($Mg(OH)_2$) and magnesium oxide (MgO) are also reported [53,54]. The removal of H_2S by MgO has been reported to be via chemical adsorption of HS and S on flat MgO(100) surfaces, where the direct interaction of H_2S with MgO is reported to be relatively weak [54]. Also, the H_2S adsorption by metal oxides alone are feasible only at higher temperatures [55]. The objective of this work is to, fabricate a composite, by impregnating nano MgO in a porous matrix such as activated carbon, which will allow to utilize both chemical and physical adsorption of H_2S thereby increasing the adsorption capacity of the sorbent at room temperature. Hence, it will be a better choice in using for the industrial applications of removing H_2S from polluted gas streams, than using the metal oxide alone. Incorporation of nano MgO with GAC to evaluate the efficacy of the composite on catalyzing H_2S has not been reported to the best of our knowledge. Therefore in this study, we impregnate nano MgO in to activated carbon, in order to ascertain the viability of this composite for H_2S adsorption. The rationale for the composite is to increase the oxygen substitution mechanism and the metal supported addition mechanism. The novel strategy employed involves the initial in-situ impregnation of nano magnesium hydroxide (nano-$Mg(OH)_2$) into GAC and then calcination of nano-$Mg(OH)_2$ to produce nano-MgO impregnated GAC.

2. Experimental

2.1. Materials and methods

Magnesium nitrate hexahydrate (98%, Research-Lab Fine Chem Industries), ammonium hydroxide (25%, Sigma-Aldrich) and absolute ethanol (≥98.8%, Sigma-Aldrich) were used as received. Polyvinylpyrrolidone (PVP, Molecular weight: 10,000, Sigma-Aldrich) as received, was used as the nonionic surfactant. Double distilled water was used in preparing all solutions. Granular activated carbon (GAC) used for the composite was from Jacobi Carbons Inc., United Kingdom. The synthesis process of nano MgO-GAC has two main steps: first, the impregnation of magnesium hydroxide nanoparticles in to GAC and second, the decomposition of impregnated magnesium hydroxide into magnesium oxide, which are summarized in Sections 2.2 to 2.5.

2.2. Synthesis of magnesium hydroxide nanoparticles and MgO nanoparticles

For the preparation of magnesium hydroxide nanoparticles, a well-established alkaline precipitation method [56] was used with some modifications. The modifications to the original procedure include the changes in reaction temperature, solvent polarity and the surfactants. $Mg(NO_3)_2.6H_2O$(s) (4 g, 0.0156 mol) was dissolved in a 20 mL mixture of double distilled water and ethanol (1:1 v/v). The nonionic surfactant, PVP (1 g, 0.0001 mol) was dissolved in another 20 mL mixture of water and ethanol (1:1). The resultant mixture was heated to 65 °C while stirring. A 5 mL amount of NH_4OH (aq) (6.5 M) was then added drop wise to the above reaction mixture with continued stirring while maintaining the temperature at 65 °C. After the complete addition of the base, the reaction mixture was allowed to cool to room temperature (27 °C), with continued stirring. The cloudy nano metal hydroxide solution was then centrifuged (Sigma 3–18) at 9000 rpm for 15 min and nano $Mg(OH)_2$(s) particles were separated. The precipitate was washed and centrifuged using a water/ethanol (1:1) mixture. The precipitate was subjected to the temperature of 360 °C in a muffle furnace (Nabertherm) to achieve MgO nanoparticles. Both synthesized nano $Mg(OH)_2$ and nano MgO were characterized using Scanning electron

microscopy (SEM), X- ray diffraction (XRD) and Thermo gravimetric analysis (TGA).

For the synthesis of magnesium oxide-activated carbon (MgO-GAC) composite pre-dried GAC (100 g) was sprayed with nano magnesium hydroxide solution (45 mL), using an in-house developed spray apparatus. For the decomposition step, the nano-$Mg(OH)_2$ impregnated GAC sample was then heated in a muffle furnace (Nabertherm) at 360 °C for 3 h. In order to prevent the combustion of GAC, the decomposition was done in N_2 environment. In order to increase the MgO content in the final composite, the GAC sample was subjected to four consequent spray cycles of $Mg(OH)_2$, followed by drying after each cycle. During the decomposition, the NH_4NO_3 by product was converted into nitrogen and water at a temperature around 250 °C [57].

2.3. Characterization of nano magnesium hydroxide and nano magnesium oxide

The surface morphology of $Mg(OH)_2$ nanoparticles was analyzed using scanning electron microscopy (Hitachi SU 6600, SEM) and transmission electron microscopy (TEM) in the scanning transmission electron microscopic mode (STEM) at 200 kV (FEI Technai G2 F20 field emission TEM). The X-ray diffraction (Bruker D8 FOCUS) patterns were recorded to obtain the crystal structure of the synthesized nanoparticles, and also to confirm the purity of the product. (Cu Kα ($\lambda = 1.5418$ Å), 40 kV and 40 mA) Thermogravimetric analysis of the synthesized magnesium hydroxide nanoparticles and the surfactant (PVP) were carried out (TA Instruments, SDT Q600) under N_2 atmosphere at a heating rate of 20 °C/min, in order to determine the calcination temperature for the nanocomposite synthesis.

2.4. Characterization of MgO-GAC composite

The scanning electron microscope was used to study the surface morphology of the four MgO-GAC composites. The XRD patterns and TGA analyses were done in the similar manner described in Section 2. The surface area and the pore structural properties of MgO-GAC composite and the virgin GAC were investigated by N_2 adsorption at 77 K (Quantachrome Autosorb iQ Surface Area Analyzer). The samples were degassed at 300 °C for 3 h, prior to each analysis and each sample was run in triplicates.

The bonding nature between MgO and GAC was assessed by synchrotron radiation (SR) based Ultra Violet photoelectron spectroscopy (UPS) and near edge X-ray absorption spectroscopy (NEXAFS). The UPS and NEXAFS measurements on GAC and MgO/GAC nanocomposite was performed at the Materials Science beamline at ELETTRA synchrotron, Trieste, Italy. Samples were outgassed in the sample load-lock until the base pressure of the load-lock fell below 5×10^{-7} mbar and then were transferred directly to the experimental chamber for measurements, in which, the base pressure with the samples inserted was ~5×10^{-10} mbar. Spectra were referenced to the binding energy (BE) of Au 4f core level recorded from a clean Au sample attached to the manipulator and were normalized to the incoming photon flux, I0, and to the number of scans. UPS spectra were recorded at normal emission (NE) mode which probes few top most layers of the sample. Therefore the survey and core level spectra recorded at their respective photon energies collect photo-emitted electrons mostly from the surface of the nanocomposite. C and O K-edge NEXAFS data were recorded in Auger electron yield (AEY) mode, using the C and O KLL Auger regions respectively, with the incident beam at normal and grazing (10°) angles to the plane of the GAC and MgO/GAC samples. The polarization of the incident SR beam is ~90% horizontal from the bending magnet source. The background of core level spectra was subtracted using 4th order polynomial function and the spectra were acquired using a SPECS Phoibos 150 hemispherical electron energy analyzer with a 1D-DLD detector. The quantification of Mg content in the four composites was done by ICP-OES analysis of acid digested composites.

2.5. H_2S adsorption studies

The H_2S testing capacity was performed according to the method, ASTM D6646. Humidified air (relative humidity 80% at room temperature) containing 1% (10,000 ppm) of H_2S was passed through a column of GAC (diameter 2.5 cm; bed height 15 cm). The test was stopped at breakthrough concentrations of 50 ppm.

The composites before and after H_2S adsorption were analyzed by Energy Dispersive X-ray spectroscopy on an SEM (Thermoscientific SEM-EDX). In order to understand the mechanism of adsorption, the differential thermogravimetric analyses (DTG) of as prepared and the exhausted composites were carried out using TA Instruments (SDT Q600) in air at a heating rate of 10 °C/min. Also, MgO-GAC composites with increasing MgO content, were prepared by increasing the number of spray cycles and the H_2S adsorption capacities in each was tested in order to get more evidence on the mechanism of H_2S adsorption.

3. Results and discussion

3.1. Characterization of magnesium hydroxide and magnesium oxide nanoparticles

The synthesis of MgO nanoparticles from nano $Mg(OH)_2$ could be considered to occur via chemical reactions as given in Eqs. (1) and (2).

$$Mg(NO_3)_2(s) + 2\ NH_4OH\ (aq) \rightarrow Mg(OH)_2 + 2\ NH_4NO_3\ (aq) \quad (1)$$

$$Mg(OH)_2(s) \rightarrow MgO\ (s) + H_2O\ (l) \quad (2)$$

Also, the base NaOH, which was used in the original method was replaced by NH_4OH in order to eliminate the possible contamination of nanocomposite by sodium (Na^+) ions. This results in NH_4NO_3 as a by-product, which is decomposed into N_2 and H_2O at 200–300 °C.

According to the TEM image (Fig. 1a) the synthesized $Mg(OH)_2$ nanoparticles are spherical in shape. The particle size varies only within the range of 2–5 nm and therefore a narrow size distribution is obtained. However, few agglomerated sites are also visible. This procedure clearly shows the synthesis of very small $Mg(OH)_2$ nanoparticles compared with previous reports [56]. This $Mg(OH)_2$ was subjected to calcination to form MgO nanoparticles. The SEM image of the MgO after calcination step reveals that the majority of the particles are in 50 nm range and in nearly a monodispersion. The shape of the particles is nearly spherical with some agglomeration sites.

The TGA analysis of nano $Mg(OH)_2$, MgO-GAC and PVP is given in the Fig. 2. The thermogravimetric analysis of as-synthesized $Mg(OH)_2$ suspension shows three weight loses around 150 °C, 375 °C and 450 °C. The weight loss at 150 °C could be attributed to the evaporation of surface bound water. The weight loss at 375 °C is due to the conversion of $Mg(OH)_2$ to MgO. The weight loss at 450 °C in the TGA profile of $Mg(OH)_2$ can be attributed to the decomposition of surfactant, which is also confirmed by the TGA profile of PVP given in Fig. 2. There are no major weight loses in the TGA profile of nano MgO composite until 700 °C, which confirms the thermal stability of the composite. A small weight loss around 714 °C is mainly due to the decomposition of carbon in the composite.

The XRD spectra obtained for nano $Mg(OH)_2$, nano MgO, MgO-GAC and virgin GAC are shown in Fig. 3. The X-ray diffraction of nano-$Mg(OH)_2$ clearly shows the peaks at the 2θ positions of 19°, 33°, 38°, 51°, 59°, 62° and 68° (Fig. 3.a) which can be assigned to (001), (100), (101), (102), (110), (111), and (013) planes respectively (ICSD). The XRD pattern of nano MgO obtained is given in fig. 3.b. This clearly shows that the highest intensity peak is at 2θ, 43° (200) crystal planes of MgO and other diffraction peaks assigned to 2θ, 37° (111), and 2θ, 62° (220) crystal planes (ICSD). However, XRD data for MgO-GAC nanocomposite reveals no distinctive peaks corresponding to nano MgO (Fig. 3c) other than two broad peaks at 2θ positions 26°and 44° which can be

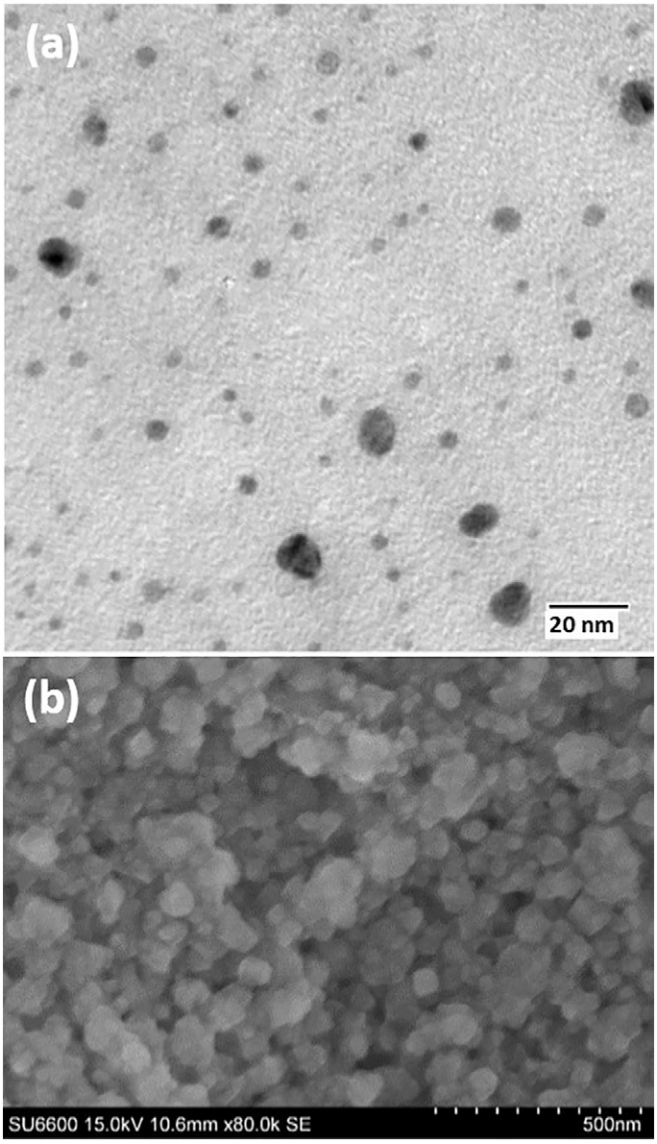

Fig. 1. (a) TEM image of $Mg(OH)_2$ nanoparticles (b) SEM image of MgO nanoparticles.

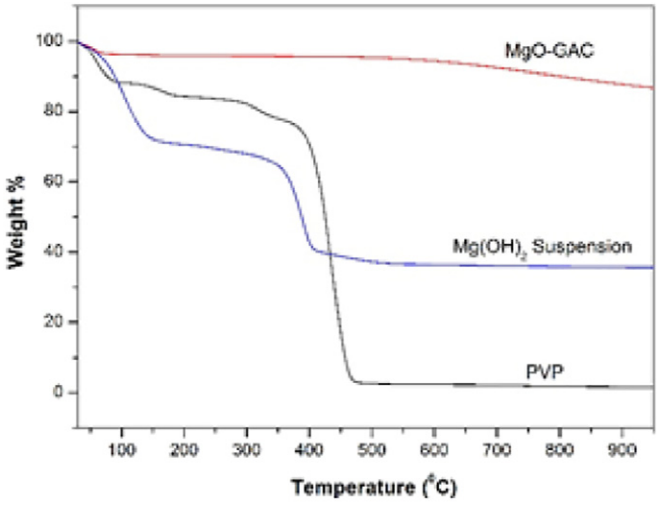

Fig. 2. TGA profiles of nano $Mg(OH)_2$ suspension, MgO-GAC composite and the surfactant (PVP).

assigned to GAC [58]. The absence of peaks corresponding to MgO can be attributed to two reasons. One reason could be that the amorphous nature of MgO nanoparticles formed on GAC [59] and the other could be due to the overlap of the main peak of MgO at 43° inside the GAC peak that appears at 44°.

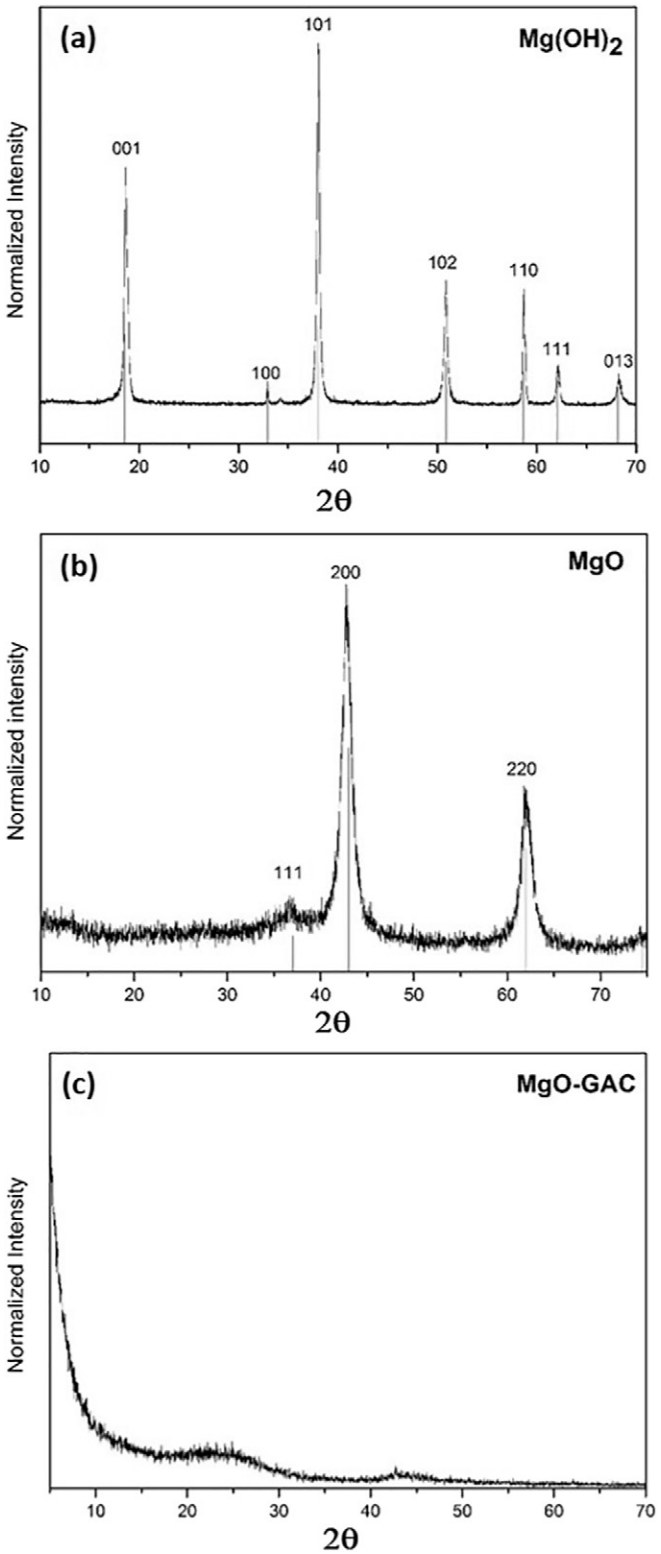

Fig. 3. XRD pattern of (a) nano-Mg(OH)2 (b) nano-MgO (c) MgO-GAC.

3.2. Morphological study of nanocomposite by SEM

Fig. 4 illustrates the SEM analysis of virgin carbon (a) and the MgO nanoparticles in the nanocomposite (b, c, d and e). However, as the images are those of localized areas, they do not provide quantitative information on the MgO content in the composite structure. Shape of the synthesized MgO nanoparticles on the surface of the GAC is nearly spherical and the narrow size of the particle size distribution is also confirmed.

3.3. Quantification of the nano-MgO in the composite

According to the ICP-OES analysis, the detected quantities of Mg quantity in the virgin carbon and the composite and the calculated respective MgO (w/w) amounts are summarized in Table 1. The calculated MgO content in the composite is 1.2% and the detected Mg content is 6900 mg/kg which is equal to MgO content of 1.15%. This proved the impregnation of nano MgO is almost 100%. However, in virgin GAC, the MgO concentration was below the detectable levels.

Table 1
MgO content and the H_2S adsorption capacity of vigin carbon and MgO-GAC composite.

Sample	Mg (mg/kg) as detected by ICP/OES	Calculated MgO (w/w) %	H_2S adsorption capacity (mg/g)
Virgin GAC	Not detected	–	53
MgO-GAC	6900	1.2	275

3.4. Bonding nature of nano-MgO with activated carbon

The permanent impregnation of nano-MgO on GAC, based on the respective core level binding energies of each element, is further confirmed by ultra violet photoelectron spectroscopy (UPS) and near edge X-ray absorption fine structure spectroscopy (NEXAFS). Fig. 5 (a-d) shows the survey and C1s, O1s and Mg2p core level spectra recorded from GAC and MgO-GAC nanocomposite. The survey spectra of GAC and GAC/MgO are dominated by the presence of a conspicuous peak at a binding energy (BE) of 285 eV. In addition, there is another noticeable peak at a BE of 533 eV. Only in the case of MgO-GAC nanocomposite, a very feeble additional response at a BE of 52 eV is seen. Further peak

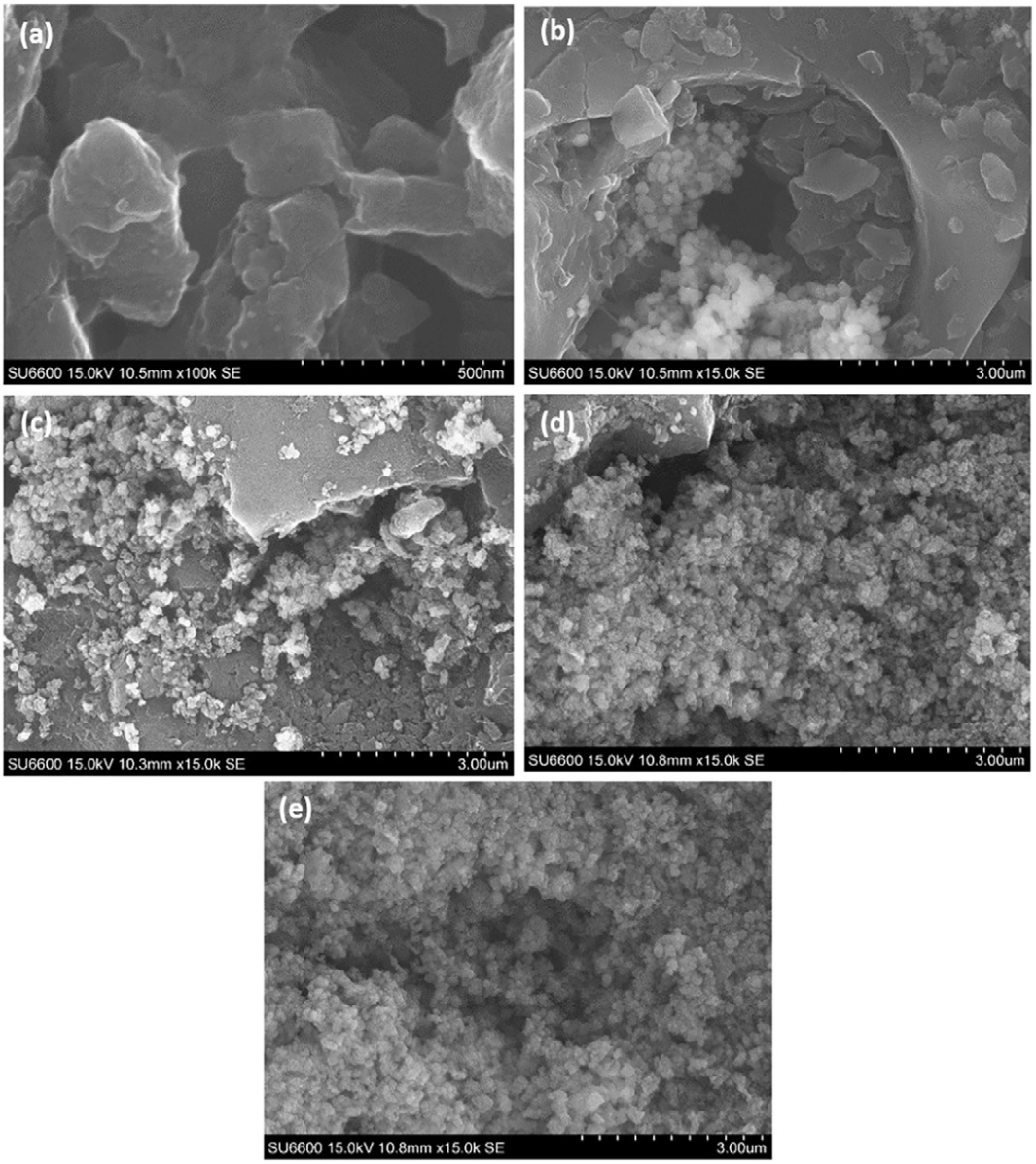

Fig. 4. SEM Images of (a) Virgin activated carbon (b,c,d,e) MgO-GAC composite.

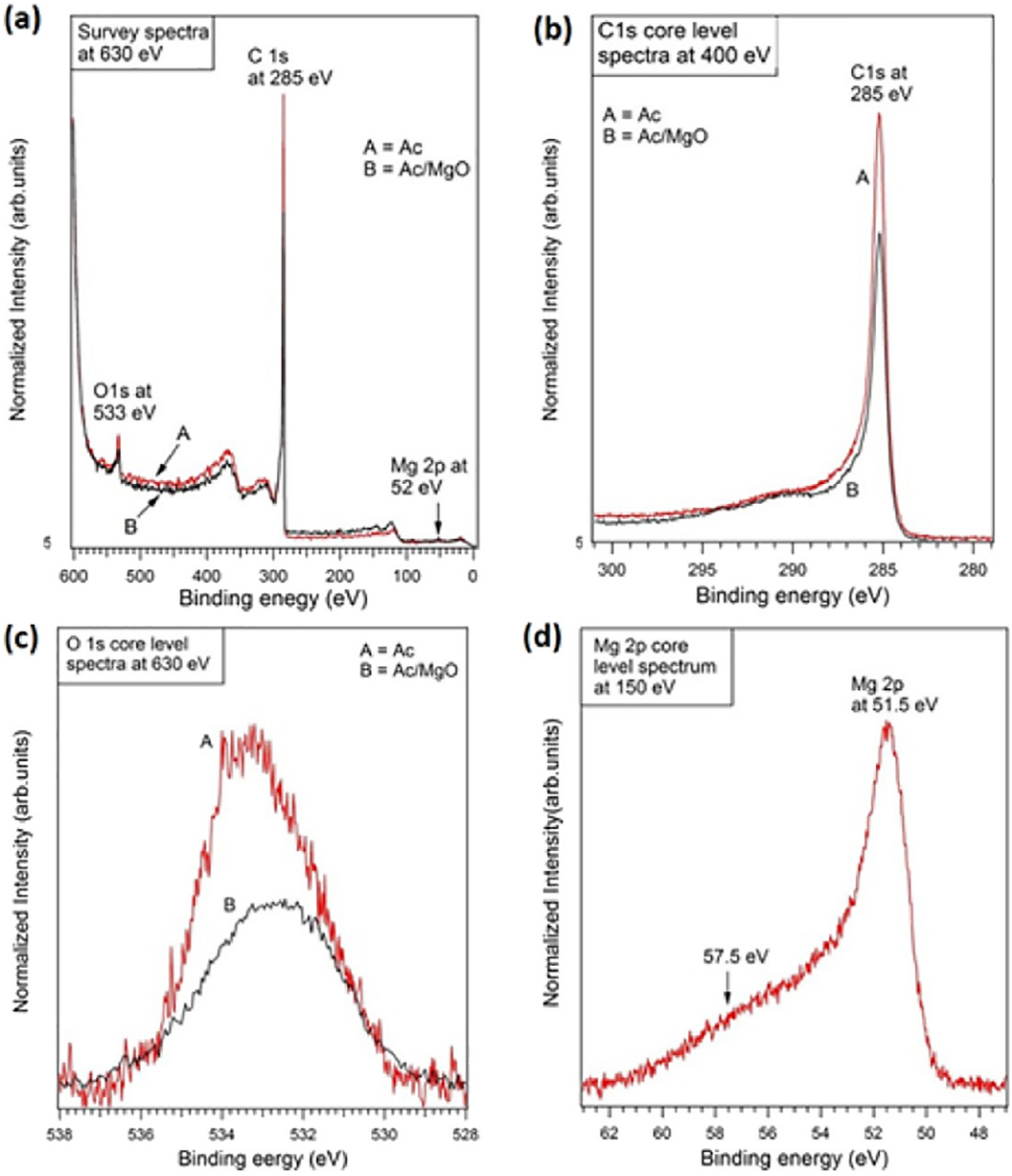

Fig. 5. Core level spectra of GAC and MgO-GAC composites: (a) full range scan from 150 to 600 eV (b) C 1 s at 400 eV (c) O 1 s at 630 eV and (d) Mg 2p at 150 eV.

intensities of the spectra recorded from MgO-GAC composite (285 and 533 eVs) are less than those recorded from GAC. Based on the information of activated carbon obtained via different processes and nature of the functional groups with various hetero atoms [60–63], the peak observed at a BE of 285 eV is assigned to the basal plane hydrocarbon C—C, or C—H [64,65]. The weak but perceptible peak seen at a BE of 533 eV is assigned to surface oxygen functional groups [60–63], The kind of surface oxygen functional group can further be identified by deconvolution of this narrow region scans, which is given in supplementary information.

The peak intensity of C 1s and O 1s for MgO/GAC nanocomposite is less than those observed for GAC, which confirms that the nano-MgO present on GAC surface as immobilized particles or as an over-layer. Because immobilized particles/over-layer could impede photo-emitted electrons from GAC (i.e., substrate/over-layer scenario) leading to a decrease in the intensity of substrate peaks. Further the decrease in intensity is also possible with scattering by nano-MgO particles. The decrease in the peak intensities for MgO/GAC nanocomposite can clearly be observed when narrow region scans of C1s and O1s are observed more closely which are shown in Fig. 5(b) and (c) confirming the presence of MgO on activated carbon. The BE position of the Mg 2p core level observed here (shown in Fig. 5(d)) is about 1 eV shifted towards higher values compared to that observed for the Mg 2p core level for ultra-thin MgO films [66]. Peak shifting to higher BEs in UPS is usually associated with surface charging effects and it is well known that MgO is a good insulating metal oxide [67]. The spectral line shape of Mg 2p observed here reveals that other oxidation states of magnesium or elements other than Mg present on the surface together with nano-MgO. Peak deconvolutions and the assignment of the peaks in Mg 2p core level spectra is given in supplementary information.

Fig. 6(a) and (b) illustrate the C and O K edge NEXAFS spectra of GAC and nano MgO/GAC composite systems. The spectra were recorded in Auger Electron Yield (AEY) mode where the intensity of the emitted primary Auger electrons is a direct measure of the X-ray absorption process. AES is highly surface sensitive technique, similar to UPS. The X-ray absorption of the carbon K edge is due to 1s–2p electronic transitions and usually consists of two energy regions associated with 1s–π* transitions at ~284–288 eV and 1s–σ* transitions at >289 eV [68]. For

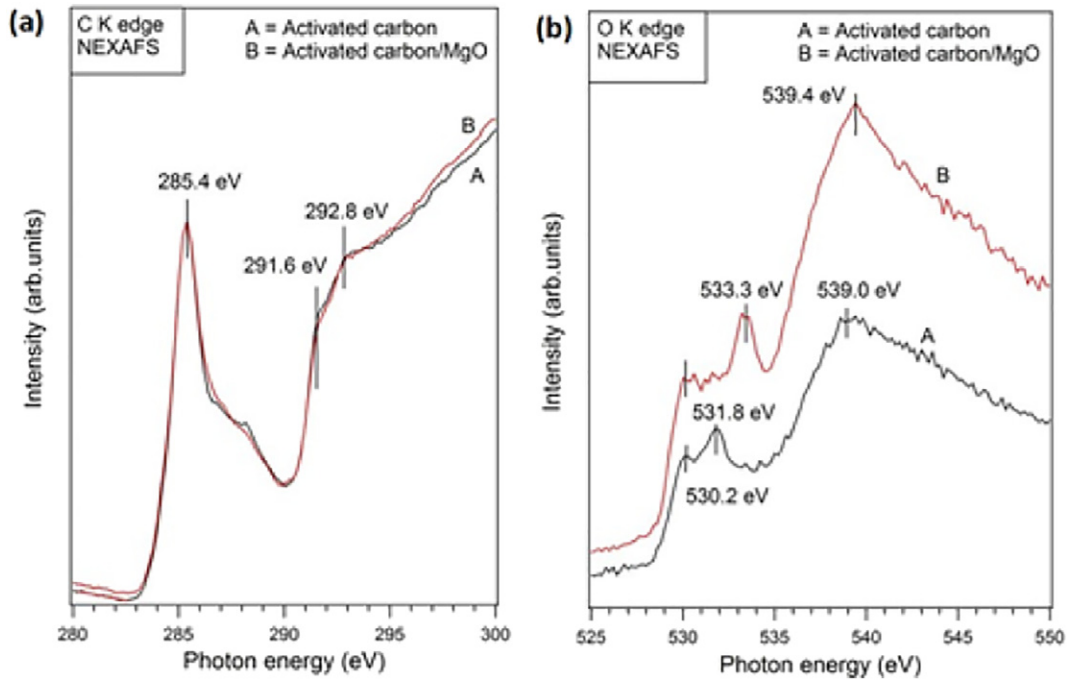

Fig. 6. K edge NEXAFS spectra of (a) GAC (b) MgO-GAC composite.

all highly ordered graphitic carbons, these transitions give rise to peaks at 285.4 and 291.7 eV, respectively [69–71]. However, one or two additional resonances in the energy range 286 to 289 eV are sometimes observed although the origin of these peaks is not universally agreed. In Fig. 6(a), a very clear resonance peak is observed at photon energy of 285.4 eV and two other small peaks at photon energies 291.6 and 292.8 eV. For GAC and MgO/GAC nanocomposite, C K edge spectra almost coincide with each other. The peak observed at 285.4 eV is undoubtedly arising due to transition from C 1s to π*. Two other small peaks observed at photon energies of 291.6 eV and 292.8 eV are interesting and originating from the transitions C1s to σ* [72]. The existence of these resonance transitions have been observed with commercially available graphite samples previously [68] and theoretical calculations show that these peaks are due to the partial overlap of the p_{xy} orbitals with p_z orbitals along c-axis of structurally non-equivalent carbon atoms that belong to two-different sub-lattices (A- and B-type carbons [68,72]). In addition, there are feeble signs for possible peaks in the energy range 286 to 298 eV as can be seen in the spectra that can be attributed to peaks in this range to C—O or C—H bonds. However, theoretical work suggests that the peaks in this range are due to the presence of defects such as atomic vacancies [73]. Given the observations made in core level spectra in this work (Supplementary information) and the variable nature of the GAC, it is probably circumspect to assign these peaks to C—O or C—H. In principle, other functional groups attached to carbon observed in core level spectra (Supplementary information) should also display their corresponding transitions within this energy range.

For oxygen functional groups on carbon materials, oxygen K-edge (543.1 eV) NEXAFS is preferred over carbon K-edge (284.2 eV) since it minimizes the strong interference from the carbon substrate. Fig. 6(b) shows O K-edge NEXAFS spectrum of GAC and MgO/GAC recorded at NE mode at room temperature. The spectra clearly demonstrate the presence of distinctive features at photon energies of 530.2, 531.8, 533.3 and 539 eV. An oxygen K-edge spectrum of oxygen containing functional group mainly consists of a pre-edge peak and a white-line (the first intense post-edge peak). By measuring known functional groups in reference compounds, it is determined that oxygen functional groups on carbon materials can be grouped into three categories, namely, carboxyl-type, carbonyl type and hydroxyl type. In general carboxyl type consists of strong pre-edge peak at about 531 eV and a broad whiteline at 539 eV, carbonyl type includes strong pre-edge peak at below 530 eV and a broad whiteline at 539 eV and hydroxyl type contains absence or very weak pre-edge peak at about 531 eV and a broad whiteline at 536–538 eV. Given that the peaks observed at a photon energy of 530.2 and 531.8 eV in this spectrum can safely be assigned to the π* state of C═O, which may belong to the carbonyl groups bonded to an aromatic ring [74] and also likely to originate from COOH groups attached at the GAC edge site [75,76] The presence of both types of these atomic groups on GAC was seen in the core level spectra. Peaks responsible for σ* state of O—H are expected to be present at about 535.5 eV [74,77] while those for the π* state of C—O from epoxide groups at about 534 eV [75]. Here we observe a clear resonance peak at 533.3 eV for MgO/GAC system, while this resonant peak is absent but an alternative peak shifted down to 531.8 eV is seen in GAC (Fig. 6B trace A). In the case of carboxyl-type functional groups, in addition to a strong pre-edge peak at about 531 eV and a broad white line at 539 eV, there also have a small second pre-edge peak at about 533 eV. As the presence of these groups for MgO/GAC is observed in the core level spectra, presumably this clear resonance peak at 533.3 eV could result from the carboxylic type (carboxyl, ester, and anhydride) functional groups associated with interactions between the MgO and GAC. The O K-edge spectral line shape of the spectra is in line with similar measurements carried out previously by other workers [73].

3.5. Surface area and the pore characteristics of the nanocomposite

Surface area and the pore structure are vital factors for the performance of the activated carbon. The surface area, pore volumes and the sizes inferred based on N_2 adsorption isotherms are summarized in the Table 2. The surface areas were calculated using the BET isotherms [78]. The total pore volume and the average pore sizes were calculated

Table 2
BET surface area and the pore structure characteristics of the nanocomposites.

Sample	BET surface area (m^2/g)	Average pore volume (cc/g)	Average pore size (Å)	Micropore volume (cc/g)
Virgin GAC	1678 ± 41	0.748 ± 0.03	8.877 ± 0.16	0.629 ± 0.01
MgO-GAC	1358 ± 39	0.595 ± 0.01	8.772 ± 0.23	0.515 ± 0.01

at the P/P_0 of 0.99. This includes all micropore, mesopore and macropore volumes. In addition, the micropore surface area and the pore volumes were calculated using the t-method by de Boer [79]. Usually, the t-method is useful in calculating the micropore volumes in the presence of mesopores, which is suitable for activated carbons.

Upon impregnation of the MgO nanoparticles, both the surface area and the pore volume tend to decrease. This is due to the blocking of pores by MgO nanoparticles as previously observed [49]. This is in line with the decrease in the average pore volume as predicted by the isotherm results. However, the average pore size of the MgO-GAC composite remain to be similar having a size around 8.8 Å. This confirms the fact that the macropores in the activated carbon, have not been clogged. On the other hand, the micropore volumes predicted by the t-method also decrease upon impregnation of MgO. Hence, the BET results confirm the successful formation of the MgO-GAC nanocomposites, having MgO nanoparticles occupy the micropores of activated carbon matrix.

3.6. H_2S adsorption capacity and the mechanism of adsorption

The H_2S gas adsorption capacity obtained using the ASTM D6646 method for the MgO-GAC sample is also summarized in the Table 1, where the adsorption capacity of the composite is 275 mg/g, whereas for virgin GAC, it remains to be 53 mg/g. This H_2S capacity shown by the MgO-GAC composite is higher than those of the copper and manganese composites of activated carbon, reported before [24,47]. The SEM-EDX analysis of the MgO-GAC composite after H_2S adsorption confirmed the presence of adsorbed sulfur, as shown in Fig. 7.

However, the quantitative analysis of the adsorbed H_2S amount using SEM-EDX is not realistic as the EDX will only give location specific results during a particular analysis.

The high level of H_2S adsorption demonstrated by this nanocomposite could be attributed to its ability to adsorb H_2S both physically and chemically. According to BET analysis, it is clear that the nanomaterial deposition has happened into the micropores which is evident by the slight decrease of micropore volume after impregnation process. In other words, it implies that the macro and mesopore structure of the activated carbon has not been clogged upon impregnation. According to Huang et al. [47] this could be considered as the non-exhaustibility of the activated carbon, thereby making the physical adsorption of H_2S molecules still possible by the composite material.

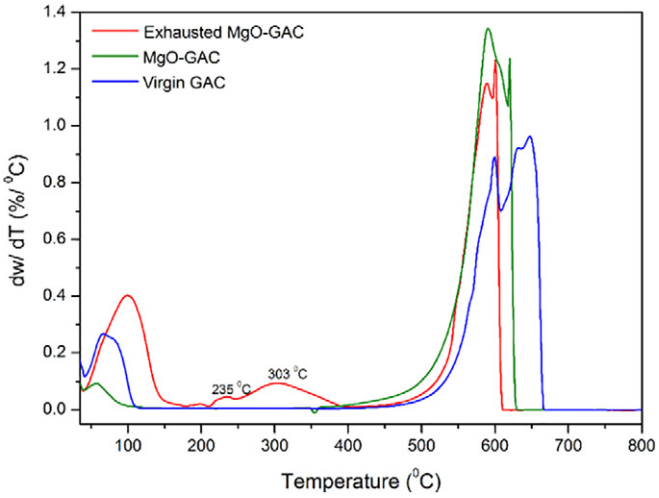

Fig. 8. DTG curves of exhausted MgO-GAC composite, as prepared MgO-GAC composite and virgin GAC.

On the other hand, the chemical adsorption of H_2S on the composite happens by substitution of O atoms by S as well as by metal supported addition mechanism. The comparison of differential thermogravimetric analyses (DTG) of virgin carbon, as prepared MgO-GAC composite and the exhausted MgO-GAC composite (i.e. after H_2S adsorption) are given in Fig. 8.

The two peaks appear around 100 °C and 600 °C in all three DTG curves are due to the loss of moisture and decomposition of carbon respectively. As the water content in the exhausted composite is higher

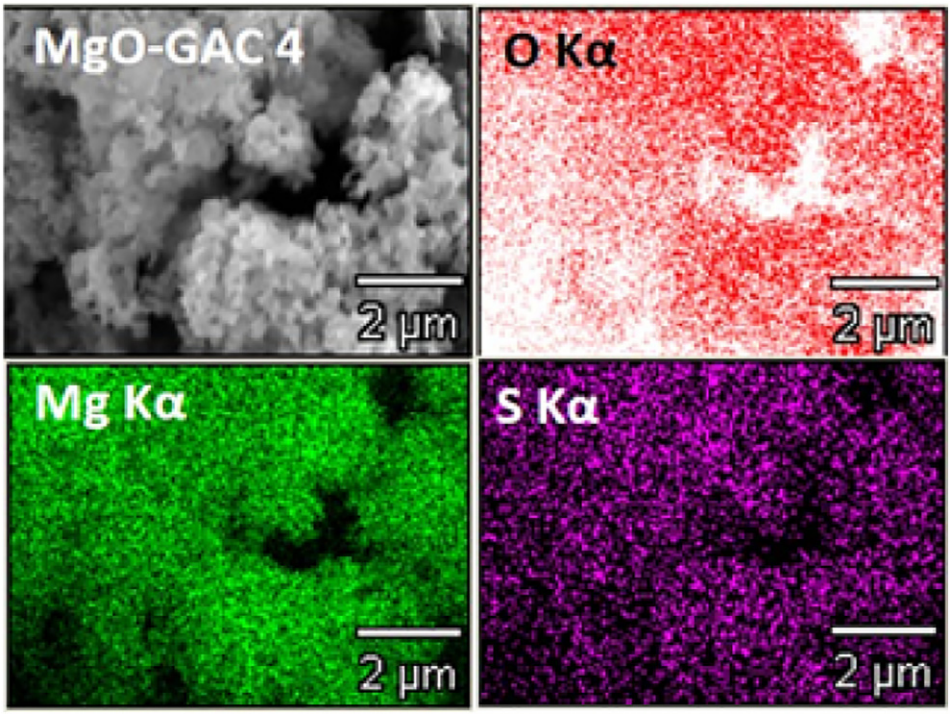

Fig. 7. SEM-EDX map of the MgO-GAC composite after H_2S adsorption.

Table 3
H_2S adsorption capacities of MgO-GAC nanocomposites with increasing MgO content.

MgO (w/w)% in the nanocomposite	H_2S adsorption capacity (mg/g)
0.2	50
0.6	125
0.9	175
1.2	275

than that of as prepared composite, it is clear that the H_2O was formed by O substitution during H_2S adsorption (Eq. (3)).

$$MgO + H_2S \rightarrow MgS + H_2O \quad (3)$$

$$Mg{-}S + O_2 \rightarrow C + SO_2 \quad (4)$$

$$MgO + H_2S \rightarrow Mg{-}S + HS \quad (5)$$

Moreover, the chemical adsorption mechanism of H_2S by O substitution is further proved by the increased H_2S adsorption capacity of the nanocomposite with the increased oxygen content in the composite (Table 3). Even though, this evidence suggest the increased nanomaterial concentration on GAC for improved chemical adsorption capacities, the maximum concentration of MgO in the final composite has to be fine-tuned in such a way, that it would not hinder the physical adsorption capacity of H_2S, because the increased nano-MgO can have a negative effect on the total pore volume of the GAC.

The two broad peaks in the region of 200 °C–400 °C, appeared only in the exhausted MgO-GAC composite, are due to the adsorbed sulfur species in two different chemical environments. As established in previous analyses, the peak at 235 °C is due to loss of sulfur dioxide (formed by an oxidation mechanism), whereas the peak at 303 °C is due to oxidation of elemental sulfur adsorbed on the catalyst [47,51]. Formation of SO_2 happens by the oxidation of elemental S on the catalyst (Eq. (4)). In addition, a metal supported addition mechanism is possible, due to the presence of metal ion sites with vacant s and p orbitals which are good potential electron acceptors for sulfur. The most likely mechanism is the site specific adsorption of H_2S by MgO (100) surfaces as suggested in some previous analyses (Eq. (5)) [53,54].

The economic feasibility and the ease of preparation of this nanocomposite make it a potential solution for H_2S removal in large scales as well. Further, the chemical modification of activated carbon introduced here, which is nano-MgO, is nontoxic and makes this composite more promising for practical applications. However, careful optimization of the MgO concentration in the composite, assessing the effects of other contaminants in laden streams on adsorption capacity and optimization of spray conditions could be identified as the future studies before scaling up the proposed method.

4. Conclusion

The nano magnesium oxide and activated carbon composite reported herein remains a novel composite for gas adsorption applications. It serves as a high capacity material for H_2S removal from gas streams. The comprehensive structural and morphological information well confirmed the efficient H_2S removal ability of the reported MgO-GAC nanocomposite. Further, the scalable adsorption capacity of this novel composite, just by varying the nano-MgO composition on the composite, makes it commercially attractive for different gas purification applications. Further improvement of this composite in terms of nanomaterial composition, size and the surface area exposed after the impregnation will undoubtedly broaden its potential commercial applications in gas adsorption.

Acknowledgements

The authors gratefully acknowledge the Jacobi Carbons Inc., UK for conducting the experiments in ICP-OES and the H_2S adsorption capacity testing for the materials synthesized during this study and Dr. Kalana Jayawardene at the Portland State University, USA for conducting Transmission Electron Spectroscopy (TEM) imaging. ARK acknowledges the ICTP-ELETTRA Users Program at the International Centre for Theoretical Physics (ICTP), Trieste, Italy for funding received to carry out SR based UPS and NEXAFS at Materials Science Beamline at ELETTRA synchrotron, Trieste, Italy.

Appendix A. Supplementary data

Supplementary data to this article can be found online at https://doi.org/10.1016/j.matdes.2017.09.034.

References

[1] M.W. Warenycia, et al., Monoamine oxidase inhibition as a sequel of hydrogen sulfide intoxication: increases in brain catecholamine and 5-hydroxytryptamine levels, Arch. Toxicol. 63 (2) (1989) 131–136.
[2] A. Maneckjee, Hydrogen Sulphide Toxicity: In Vitro Effects on Cholinergic Nervous System Components Acetylcholinesterase and Nicotinic Receptor Sites, St. Francis Xavier University, 1985.
[3] R.O. Beauchamp, et al., A critical review of the literature on hydrogen sulfide toxicity, CRC Crit. Rev. Toxicol. 13 (1) (1984) 25–97.
[4] I.M.F. Arnold, et al., Health implication of occupational exposures to hydrogen sulfide, J. Occup. Environ. Med. 27 (5) (1985) 373–376.
[5] R.E. Rogers, J. Ferin, Effect of hydrogen sulfide on bacterial inactivation in the rat lung, Arch. Environ. Health 36 (5) (1981) 261–264.
[6] L.J. Hayden, H. Goeden, S.H. Roth, Growth and development in the rat during subchronic exposure to low levels of hydrogen sulfide, Toxicol. Ind. Health 6 (3–4) (1990) 389–401.
[7] L.J. Hayden, H. Goeden, S.H. Roth, Exposure to low levels of hydrogen sulfide elevates circulating glucose in maternal rats, J. Toxicol. Environ. Health 31 (1) (1990) 45–52.
[8] B. Ramazzini, W.C. Wright, Diseases of workers: translated from the Latin text De Morbis Artifactum of 1713 by Wilmer Care Wright, History of medicine, Hafner, 1964.
[9] R.J. Reiffenstein, W.C. Hulbert, S.H. Roth, Toxicology of hydrogen sulfide, Annu. Rev. Pharmacol. Toxicol. 32 (1) (1992) 109–134.
[10] T.W. Lambert, et al., Hydrogen sulfide (H2S) and sour gas effects on the eye. A historical perspective, Sci. Total Environ. 367 (1) (2006) 1–22.
[11] M. Tolonen, et al., A follow-up study of coronary heart disease in viscose rayon workers exposed to carbon disulphide, Br. J. Ind. Med. 32 (1) (1975) 1–10.
[12] P. Jäppinen, S. Tola, Cardiovascular mortality among pulp mill workers, Br. J. Ind. Med. 47 (4) (1990) 259–262.
[13] D.H. Truong, et al., Molecular mechanisms of hydrogen sulfide toxicity, Drug Metab. Rev. 38 (4) (2006) 733–744.
[14] T.H. Milby, R.C. Baselt, Hydrogen sulfide poisoning: clarification of some controversial issues, Am. J. Ind. Med. 35 (2) (1999) 192–195.
[15] R.P. Smith, Hydrogen sulfide poisoning, Can. Med. Assoc. J. 118 (7) (1978) 775–776.
[16] Meuly, W.C., Process for the removal of hydrogen sulfide from gaseous streams by catalytic oxidation of hydrogen sulfide to sulfur while inhibiting the formation of sulfur oxides. 1977, Google Patents.
[17] Shafer, R.E., Method of removing H2 S from a gas stream utilizing boron-vanadium and iron complexes. 1983, Google Patents.
[18] Chou, C.C., Method of removing hydrogen sulfide from gases. 1984, Google Patents.
[19] Zarchy, A.S., R. Correia, and C.C. Chao, Process for the adsorption of hydrogen sulfide with clinoptilolite molecular sieves. 1992, Google Patents.
[20] L. Lu, J.T.W. Yeow, An adsorption study of indoxyl sulfate by zeolites and polyethersulfone–zeolite composite membranes, Mater. Des. 120 (Supplement C) (2017) 328–335.
[21] Hufton, J.R., et al., Gas purification by adsorption of hydrogen sulfide. 2013, Google Patents.
[22] Y. Yang, E.R. Allen, Biofiltration control of hydrogen sulfide 1. Design and operational parameters, Air Waste 44 (7) (1994) 863–868.
[23] M. Yumura, E. Furimsky, Comparison of calcium oxide, zinc oxide, and iron(III) oxide hydrogen sulfide adsorbents at high temperatures, Ind. Eng. Chem. Process. Des. Dev. 24 (4) (1985) 1165–1168.
[24] Y.-J. Liu, et al., Thermal regeneration of manganese supported on activated carbons treated by HNO3 for desulfurization, Energy Fuel 29 (3) (2015) 1931–1940.
[25] R.I. Hegde, J.M. White, Chemisorption and decomposition of hydrogen sulfide on rhodium(100), J. Phys. Chem. 90 (2) (1986) 296–300.
[26] T.L. Slager, C.H. Amberg, Infrared investigation of H2S adsorption and decomposition on alumina and on alumina supported molybdenum sulfide, Can. J. Chem. 50 (21) (1972) 3416–3423.
[27] W. Feng, et al., Adsorption of hydrogen sulfide onto activated carbon fibers: effect of pore structure and surface chemistry, Environ. Sci. Technol. 39 (24) (2005) 9744–9749.

[28] L.M. Le Leuch, A. Subrenat, P. Le Cloirec, Hydrogen sulfide adsorption and oxidation onto activated carbon cloths: Applications to odorous gaseous emission treatments, Langmuir 19 (26) (2003) 10869–10877.
[29] P.-W. Xiao, et al., Biomass-derived flexible porous carbon materials and their applications in supercapacitor and gas adsorption, Mater. Des. 129 (2017) 164–172.
[30] W. Tang, et al., Preparation of a novel porous adsorption material from coal slag and its adsorption properties of phenol from aqueous solution, Mater. Des. 88 (Supplement C) (2015) 1191–1200.
[31] C.P. Huang, D.W. Blankenship, The removal of mercury(II) from dilute aqueous solution by activated carbon, Water Res. 18 (1) (1984) 37–46.
[32] A. Bhatnagar, et al., An overview of the modification methods of activated carbon for its water treatment applications, Chem. Eng. J. 219 (2013) 499–511.
[33] A. Netzer, D.E. Hughes, Adsorption of copper, lead and cobalt by activated carbon, Water Res. 18 (8) (1984) 927–933.
[34] S. Bashkova, et al., Activated carbon catalyst for selective oxidation of hydrogen sulphide: on the influence of pore structure, surface characteristics, and catalytically-active nitrogen, Carbon 45 (6) (2007) 1354–1363.
[35] R. Reich, W.T. Ziegler, K.A. Rogers, Adsorption of methane, ethane, and ethylene gases and their binary and ternary mixtures and carbon dioxide on activated carbon at 212-301 K and pressures to 35 atmospheres, Ind. Eng. Chem. Process. Des. Dev. 19 (3) (1980) 336–344.
[36] L. Pei, J. Zhou, L. Zhang, Preparation and properties of Ag-coated activated carbon nanocomposites for indoor air quality control, Build. Environ. 63 (2013) 108–113.
[37] T. Dobre, et al., Volatile organic compounds removal from gas streams by adsorption onto activated carbon, Ind. Eng. Chem. Res. 53 (9) (2014) 3622–3628.
[38] M.A. Daley, et al., Adsorption of SO2 onto oxidized and heat-treated activated carbon fibers (ACFs), Carbon 35 (3) (1997) 411–417.
[39] J. Masuda, J. Fukuyama, S. Fujii, Influence of concurrent substances on removal of hydrogen sulfide by activated carbon, Chemosphere 39 (10) (1999) 1611–1616.
[40] X. Wu, et al., Desulfurization of gaseous fuels using activated carbons as catalysts for the selective oxidation of hydrogen sulfide, Energy Fuel 19 (5) (2005) 1774–1782.
[41] T.J. Bandosz, On the adsorption/oxidation of hydrogen sulfide on activated carbons at ambient temperatures, J. Colloid Interface Sci. 246 (1) (2002) 1–20.
[42] A. Bagreev, H. Rahman, T.J. Bandosz, Study of H2S adsorption and water regeneration of spent coconut-based activated carbon, Environ. Sci. Technol. 34 (21) (2000) 4587–4592.
[43] A. Bagreev, T.J. Bandosz, H2S adsorption/oxidation on unmodified activated carbons: importance of prehumidification, Carbon 39 (15) (2001) 2303–2311.
[44] M.P. Cal, B.W. Strickler, A.A. Lizzio, High temperature hydrogen sulfide adsorption on activated carbon: I. Effects of gas composition and metal addition, Carbon 38 (13) (2000) 1757–1765.
[45] R. Yan, et al., Kinetics and mechanisms of H2S adsorption by alkaline activated carbon, Environ. Sci. Technol. 36 (20) (2002) 4460–4466.
[46] J.-H. Tsai, F.-T. Jeng, H.-L. Chiang, Removal of H2S from exhaust gas by use of alkaline activated carbon, Adsorption 7 (4) (2001) 357–366.
[47] C.-C. Huang, C.-H. Chen, S.-M. Chu, Effect of moisture on H2S adsorption by copper impregnated activated carbon, J. Hazard. Mater. 136 (3) (2006) 866–873.
[48] T.J. Bandosz, Effect of pore structure and surface chemistry of virgin activated carbons on removal of hydrogen sulfide, Carbon 37 (3) (1999) 483–491.
[49] D.-Y. Choi, et al., Adsorption dynamics of hydrogen sulfide in impregnated activated carbon bed, Adsorption 14 (4–5) (2008) 533–538.
[50] J.P. Boudou, et al., Adsorption of H2S or SO2 on an activated carbon cloth modified by ammonia treatment, Carbon 41 (10) (2003) 1999–2007.
[51] F. Adib, A. Bagreev, T.J. Bandosz, Adsorption/oxidation of hydrogen sulfide on nitrogen-containing activated carbons, Langmuir 16 (4) (2000) 1980–1986.
[52] T.J. Bandosz, et al., Silica−polyamine-based carbon composite adsorbents as media for effective hydrogen sulfide adsorption/oxidation, Chem. Mater. 19 (10) (2007) 2500–2511.
[53] J.A. Rodriguez, et al., Studies on the behavior of mixed-metal oxides and desulfurization: reaction of H2S and SO2 with Cr2O3(0001), MgO(100), and CrxMg1-xO(100), J. Am. Chem. Soc. 122 (49) (2000) 12362–12370.
[54] J.A. Rodriguez, T. Jirsak, S. Chaturvedi, Reaction of H2S with MgO(100) and Cu/MgO(100) surfaces: band-gap size and chemical reactivity, J. Chem. Phys. 111 (17) (1999) 8077–8087.
[55] K. Polychronopoulou, J.L.G. Fierro, A.M. Efstathiou, Novel Zn–Ti-based mixed metal oxides for low-temperature adsorption of H2S from industrial gas streams, Appl. Catal. B Environ. 57 (2) (2005) 125–137.
[56] J.Y. Park, et al., Chemical synthesis and characterization of highly oil dispersed MgO nanoparticles, J. Ind. Eng. Chem. 12 (6) (2006) 882–887.
[57] J. Jurado, J.R.J. Egea, Processing of and Microstructure-property Relations in SOFC Components and Ceramic Gas-separation Membranes, Consejo Superior de Investigaciones Científicas, 2002.
[58] S. Mopoung, Surface image of charcoal and activated charcoal from banana peel, J. Microsc. Soc. Thailand 22 (2008) 15–19.
[59] M.S. Fernando, R.M. de Silva, K.M.N. de Silva, Synthesis, characterization, and application of nano hydroxyapatite and nanocomposite of hydroxyapatite with granular activated carbon for the removal of Pb2+ from aqueous solutions, Appl. Surf. Sci. 351 (2015) 95–103.
[60] Y. El-Sayed, T.J. Bandosz, Adsorption of valeric acid from aqueous solution onto activated carbons: role of surface basic sites, J. Colloid Interface Sci. 273 (1) (2004) 64–72.
[61] M.S. Shafeeyan, et al., A review on surface modification of activated carbon for carbon dioxide adsorption, J. Anal. Appl. Pyrolysis 89 (2) (2010) 143–151.
[62] V.L. Snoeyink, W.J. Weber, The surface chemistry of active carbon; a discussion of structure and surface functional groups, Environ. Sci. Technol. 1 (3) (1967) 228–234.
[63] H.M.a.F. Rodriguez-Reinoso, Activated Carbon, Elsevier Ltd, 2006.
[64] D.E. Wurster, K.A. Alkhamis, L.E. Matheson, Prediction of adsorption from multicomponent solutions by activated carbon using single-solute parameters, AAPS PharmSciTech 1 (3) (2000) 79–93.
[65] P.L. Gai, B.H.M. Billinge, A.M. Brown, Proceedings of the conference on porosity and carbon materials: measurements and applications microstructure of carbons, Carbon 27 (1) (1989) 41–53.
[66] J.S. Corneille, J.-W. He, D.W. Goodman, XPS characterization of ultra-thin MgO films on a Mo(100) surface, Surf. Sci. 306 (3) (1994) 269–278.
[67] O.E. Taurian, M. Springborg, N.E. Christensen, Self-consistent electronic structures of MgO and SrO, Solid State Commun. 55 (4) (1985) 351–355.
[68] A.S. Milev, et al., Unoccupied electronic structure of ball-milled graphite, Phys. Chem. Chem. Phys. 12 (25) (2010) 6685–6691.
[69] D.A. Fischer, et al., Graphitic interlayer states: a carbon \textit{K} near-edge x-ray-absorption fine-structure study, Phys. Rev. B 44 (3) (1991) 1427–1429.
[70] R. Ahuja, et al., Theoretical and experimental study of the graphite 1 \textit{s} X-ray absorption edges, Phys. Rev. B 54 (20) (1996) 14396–14404.
[71] P.E. Batson, Carbon 1 \textit{s} near-edge-absorption fine structure in graphite, Phys. Rev. B 48 (4) (1993) 2608–2610.
[72] D.G. McCulloch, R. Brydson, Carbon K-shell near-edge structure calculations for graphite using the multiple-scattering approach, J. Phys. Condens. Matter 8 (21) (1996) 3835.
[73] V.A. Coleman, et al., Defect formation in graphene nanosheets by acid treatment: an X-ray absorption spectroscopy and density functional theory study, J. Phys. D. Appl. Phys. 41 (6) (2008), 062001.
[74] J.T. Francis, A.P. Hitchcock, Inner-shell spectroscopy of p-benzoquinone, hydroquinone, and phenol: distinguishing quinoid and benzenoid structures, J. Phys. Chem. 96 (16) (1992) 6598–6610.
[75] H.K. Jeong, et al., X-ray absorption spectroscopy of graphite oxide, Europhys. Lett. 82 (6) (2008) 67004.
[76] V. Lee, et al., Large-area chemically modified graphene films: electrophoretic deposition and characterization by soft X-ray absorption spectroscopy, Chem. Mater. 21 (16) (2009) 3905–3916.
[77] L.Å. Näslund, et al., X-ray absorption spectroscopy measurements of liquid water, J. Phys. Chem. B 109 (28) (2005) 13835–13839.
[78] S. Brunauer, P.H. Emmett, E. Teller, Adsorption of gases in multimolecular layers, J. Am. Chem. Soc. 60 (2) (1938) 309–319.
[79] J.H. de Boer, et al., Studies on pore systems in catalysts: VII. Description of the pore dimensions of carbon blacks by the t method, J. Catal. 4 (6) (1965) 649–653.